JACS
JOURNAL OF THE AMERICAN CHEMICAL SOCIETY
pubs.acs.org/JACS
Article

Nanoarchitecture through Strained Molecules: Cubane-Derived Scaffolds and the Smallest Carbon Nanothreads

Haw-Tyng Huang,* Li Zhu, Matthew D. Ward, Tao Wang, Bo Chen, Brian L. Chaloux, Qianqian Wang, Arani Biswas, Jennifer L. Gray, Brooke Kuei, George D. Cody, Albert Epshteyn, Vincent H. Crespi, John V. Badding, and Timothy A. Strobel*

Cite This: J. Am. Chem. Soc. 2020, 142, 17944−17955

Read Online

ACCESS | Metrics & More | Article Recommendations | Supporting Information

ABSTRACT: Relative to the rich library of small-molecule organics, few examples of ordered extended (i.e., nonmolecular) hydrocarbon networks are known. In particular, sp^3 bonded, diamond-like materials represent appealing targets because of their desirable mechanical, thermal, and optical properties. While many covalent organic frameworks (COFs)—extended, covalently bonded, and porous structures—have been realized through molecular architecture with exceptional control, the design and synthesis of dense, covalent extended solids has been a longstanding challenge. Here we report the preparation of a sp^3-bonded, low-dimensional hydrocarbon synthesized via high-pressure, solid-state diradical polymerization of cubane (C_8H_8), which is a saturated, but immensely strained, cage-like molecule. Experimental measurements show that the obtained product is crystalline with three-dimensional order that appears to largely preserve the basic structural topology of the cubane molecular precursor and exhibits high hardness (comparable to fused quartz) and thermal stability up to 300 °C. Among the plausible theoretical candidate structures, one-dimensional carbon scaffolds comprising six- and four-membered rings that pack within a pseudosquare lattice provide the best agreement with experimental data. These diamond-like molecular rods with extraordinarily small thickness are among the smallest members in the carbon nanothread family, and calculations indicate one of the stiffest one-dimensional systems known. These results present opportunities for the synthesis of purely sp^3-bonded extended solids formed through the strain release of saturated molecules, as opposed to only unsaturated precursors.

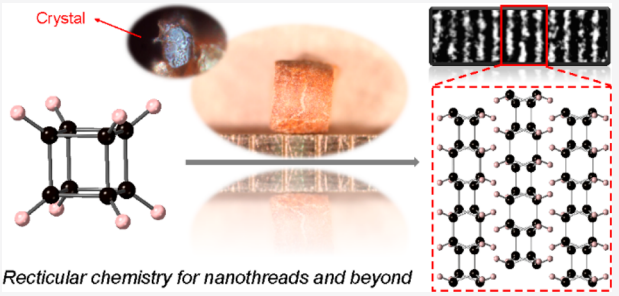

Recticular chemistry for nanothreads and beyond

INTRODUCTION

Theoretical studies predict numerous extended carbon networks that remain unsynthesized.[1−3] In particular, extended networks of sp^3 carbon similar to diamond represent appealing targets, yet have proven to be exceedingly challenging to synthesize.[4,5] An alternative approach for realizing such extended networks is high-pressure, solid-state polymerization of carbon-rich molecules. For instance, unsaturated hydrocarbons such as aromatics or acetylene have been suggested to stabilize graphane (hydrographene) structures.[6,7] Our previous work also identified a three-dimensional sp^3 bonded "K4"-like crystalline hydrocarbon from a polymerized acetylene-benzene cocrystal.[8,9] High-pressure solid-state polymerization of molecules offers access to unique, kinetically stabilized chemical structures that are typically inaccessible by other methods.[6−8,10] Unlike porous polymers or covalent organic frameworks (COFs),[11,12] which are constructed by linking molecular building blocks via conventional chemistry, these dense covalent structures are formed when the chemical interactions of molecular systems are dramatically altered by extreme pressure.[13] Thus, materials formed under high-pressure are typically dense extended solids.[14−16]

The discovery of sp^3-bonded carbon nanothread structures formed by the controlled compression of aromatic precursors such as benzene has stimulated interest in the rational design of 1D nanomaterials accessible via high-pressure solid-state chemistry.[17−20] The doping and functionalization of nanothreads can be precisely engineered by introducing precursors with heteroatoms[21] or exterior functional groups.[22] Nanothreads therefore collectively function as both nanomaterials and chemically versatile hydrocarbon molecules. These materials are predicted to uniquely combine lightweight and high tensile strength/stiffness with elasticity.[23−25] In addition, arrays of narrow, stiff, and straight nanothreads exhibit promise for advanced mechanical and thermal properties as bulk materials, useful in a diverse range of applications.[26−28]

Although multiple molecules are known to undergo pressure-induced polymerization into nanothreads,[19,21,22,29]

Received: November 15, 2019
Published: January 21, 2020

Downloaded via PENNSYLVANIA STATE UNIV on October 22, 2020 at 21:05:53 (UTC).
See https://pubs.acs.org/sharingguidelines for options on how to legitimately share published articles.

© 2020 American Chemical Society

https://dx.doi.org/10.1021/jacs.9b12352
J. Am. Chem. Soc. 2020, 142, 17944−17955

the synthesis of a single-crystalline nanothread array with full three-dimensional order has not been achieved. A single-point defect can disrupt the long-range axial order, and thus only a few nanometers of axial translational order has previously been observed in nanothread crystals.[19,30] Aromatic molecules examined to date typically form nanothread composites consisting of ∼80% fully saturated degree-6 threads mixed with partially saturated degree-4 threads, as well as disordered material.[31] Unlike aromatics, saturated molecules exhibit extraordinary chemical stability under high pressure and are therefore usually not considered as reactive precursors. This is because of the non-negative volume of activation associated with the polymerization of these molecules, which requires bond cleavage before new bond formation can occur.[32−34] However, an alternative way to synthesize a pure sp^3-bonded material is through radical polymerization of strained and saturated molecules.[35−37] For example, anionic addition polymerization of propellane results in rod-shaped "n-staffane" molecules.[36] The central inverse C−C bond of propellane is cleaved and connected to adjacent monomers, resulting in a rigid molecular rod.[37] Recently, hypothetical nanothread architectures built from adamantane have also been proposed to have higher mechanical strengths than benzene nanothreads.[38] Similarly, cubane, which is an immensely strained C_xH_x molecule with 90° C−C−C bond angles and 100% sp^3 hybridization, should polymerize to form entirely sp^3 bonded structures. The preparation of poly cubyl rods (or [n]-cubylcubanes) generally requires single-electron transfer between the 1,4-sites,[39] leading to dimers and oligomers with freely rotating skeletons.[39,40] With the recent scalable synthesis of cubane derivatives, cubane-derived porous frameworks displaying selective adsorption of hydrocarbons have been demonstrated.[41]

Despite its immense strain energy, cubane is surprisingly inert to pressure at room temperature, as reported in our previous work.[34] This inertness is attributed to a high energy of activation associated with any prospective polymerization reaction. The small volume change associated with the bond cleavage and reformation event required for cubane polymerization leads to a small $P\Delta^{\ddagger}V$ work, which is not sufficient to overcome the energy barrier and therefore results in robust kinetic stability under room-temperature compression. We herein demonstrate that a crystalline array of strained cubane molecules can nevertheless be thermally activated and subsequently polymerize into a crystalline extended hydrocarbon network. Elevated temperature provides thermal activation for the high-pressure polymerization reaction. At temperature just above the isomerization temperature, the $-T\Delta^{\ddagger}S$ term becomes significantly more negative, which lowers the $\Delta^{\ddagger}G$ barrier.[32] Furthermore, pressure greatly enhances intermolecular interactions, which guide the reaction toward novel cubane-derived scaffolds not yet realized. Distinct from previously synthesized cubane-derived porous frameworks,[41] the *poly*-cubane synthesized here is dense and composed of carbons bonded with tetrahedral connectivity. These cubane-derived threads have a subnanometer thickness of ∼2 Å, and thus represent one of the narrowest sp^3 frameworks constructed by 4-fold-coordinated carbons with tetrahedral angles.

EXPERIMENTAL METHODS

Precursor Synthesis. Cubane was synthesized by a two-step, one-pot Barton decarboxylation of 1,4-cubanedicarboxylic acid (Boron Molecular, >97%) as previously reported.[34,42,43] Briefly, 1,4-cubanedicarboxylic acid (1.0167 g, 5.291 mmol) was suspended in a round-bottom flask with 25 mL of $CHCl_3$. A catalytic amount of DMF and oxalyl chloride were added to the flask and the mixture heated and stirred in an oil bath at 65 °C for 2 h, after which all solids had dissolved and bubbling had ceased. Separately, sodium pyrithione and catalytic DMAP were added to 25 mL of THF. The solution of cubane-1,4-bis(acid chloride) in $CHCl_3$ was transferred to the sodium pyrithione suspension and the mixture irradiated with UV light (∼350 nm, 35 W) for 16 h under a N_2 blanket. Volatiles were removed and the remaining solids were taken up in dilute HCl and *n*-pentane. The yellow pentane fraction was dried over $MgSO_4$, and volatiles distilled into a liquid nitrogen-cooled trap under static vacuum.

Sample Loading. Cubane samples along with pressure calibrants (ruby or gold particles) were loaded into DACs with culet sizes ranging between 300 and 1000 μm. The DAC was prepared by preindenting a Re gasket to a thickness between 40 and 50 μm or a thin stainless-steel gasket to approximately 100 μm. The sample chamber was prepared by drilling a hole into the center of indentation with the size of roughly one-half of the diamond culet diameter. Pressure was calibrated by measuring the florescence of ruby.[44] The equation of state of Au served as a secondary pressure calibration in order to determine pressure when internal stresses within the ruby crystal gave exaggerated values.[45] All samples were sealed to a low starting pressure (<2 GPa) within the inert atmosphere of an argon glovebox without any pressure medium.

High-Pressure Synthesis. Polycrystalline cubane was compressed in the DAC to various pressures between 2−30 GPa. Samples were held at the target pressure and heated to 250 °C for 24 h, after which they were cooled to ambient temperature and the pressure was released to ambient. The synthesis temperature (250 °C) was selected to be just above the cubane isomerization temperature, which has been shown to be sufficient to overcome the barrier against symmetry-forbidden isomerization of cubane at ambient pressure.[46,47] Additional synthesis runs were performed using a large-volume multianvil apparatus at 12 GPa and ca. 250 °C, using a standardized 14-8 assembly[48] with a Cr-doped MgO octahedron, ZrO_2 insulator, graphite heater, and hexagonal boron nitride (*h*-BN) capsule.

X-ray Scattering. X-ray diffraction patterns were collected at GSECARS beamline 13-IDD, and the High-Pressure Collaborative Access Team (HPCAT) beamlines 16-IDB and 16-BMD of the Advanced Photon Source (APS) at Argonne National Laboratory. At beamline 16-IDB and 16-BMD, a monochromatic beam of λ = 0.4066 or 0.4246 Å was focused on the sample, and diffraction patterns were recorded on a MAR image plate. 2-D diffraction patterns were processed and converted to 1-D patterns with intensity versus 2θ or intensity versus momentum transfer, Q, using the program DIOPTAS.[49] Beamline 13-IDD used a wavelength of 0.3344 Å, and the X-ray beam was focused to ∼2 × 2 μm^2 using Kirkpatrick-Baez mirrors. The microbeam was exceptionally useful for collecting diffraction patterns from microcrystals. In addition, high-energy, high-flux monochromatic X-ray scattering for high-resolution PDF analysis was performed at beamline 11-IDB. A collimated 25 × 25 μm^2 beam at λ = 0.2113 Å (ca. 58 keV) was used to avoid clipping the Re gasket hole edge. The high flux and energy of ∼58 keV, which corresponds to a peak in the undulator spectrum, provided strong elastic scattering and a large Q range (0.5 to 23 $Å^{-1}$) for high-fidelity PDF analysis.

Transmission Electron Microscopy. Samples were imaged using an FEI Titan Krios G2 Cryo-TEM equipped with a spherical aberration corrector and two direct electron detectors: the Falcon 3EC direct electron camera and the K2 direct electron detector, strategically designed for low-dose imaging and spectroscopy, respectively. Hydrocarbon samples are susceptible to electron beam damage. Therefore, samples were imaged using the 300 kV TEM platform under cryogenic conditions to minimize radiolysis damage. The high-resolution images were collected at a dose rate of 40 $e^-/Å^2s$ with a total accumulated dose of 480 $e^-/Å^2s$ using the Falcon 3EC direct electron camera. Electron energy loss spectroscopy (EELS) was performed in diffraction mode at a dose rate of 1.2 $e^-/Å^2s$ with an

https://dx.doi.org/10.1021/jacs.9b12352
J. Am. Chem. Soc. 2020, 142, 17944−17955

accumulated dose of 24 $e^-/Å^2$ using the Gatan postcolumn Quantum 968 energy filter on the Krios, which includes the K2 Summit direct electron detector. Such ultralow dose conditions in combination with a cryogenic environment mitigate e-beam induced sample damage such as hybridization changes and amorphization, and direct electron detection enables high-resolution imaging under these ultralow dose conditions. The recovered samples were observed to be more stable under the electron beam than conventional saturated hydrocarbons and benzene nanothreads, possibly because of the high degree of structural order and close packing.

Calculations. Geometry relaxations of the candidate crystal structures were performed using density functional theory as implemented in the VASP package.[50] The PBE exchange-correlation functional,[51,52] and the projector-augmented wave method were used.[53,54] Dispersion correction was included by the Becke-Jonson damping DFT-D3(BJ) method of Grimme.[55,56] The energy cutoff for the plane-wave basis was 600 eV. A 0.2 eV Gaussian smearing and a k-point mesh of 0.5 $Å^{-1}$ were used. Metadynamics simulations[57] were employed to study the polymerization mechanism in solid cubane, using scaled components of the edge vectors of the simulation cell as collective variables and the evolution of the simulation cell with the derivative of the Gibbs free energy with respect to the six collective variables. Ab initio molecular dynamics simulations were also performed under both uniaxial stress and hydrostatic compression to investigate the reaction. Further details are provided in the Supporting Information.

RESULTS AND DISSCUSSION

Synthesis and Characterization of Polycubane. After compression (4−30 GPa) and gentle heating at 250 °C, the colorless cubane samples transform to a translucent yellow. The color change is irreversible, signifying the occurrence of a chemical reaction. Unlike volatile molecular cubane, the recovered samples do not sublime (even under the high vacuum inside the TEM column, $<10^{-7}$ torr), indicating that they are no longer composed of small molecules. Powder X-ray diffraction (PXRD) measurements reveal that the material is highly crystalline, and micron-sized single-crystalline domains can be visualized by optical and electron microscopy. In situ temperature-dependent PXRD shows that the recovered crystalline lattice remains stable up to 300 °C (Figure S1). This is much higher than the melting point of solid cubane (132 °C) but similar to rigid-rod hydrocarbon molecules.[58,59] These results indicate that a high-pressure, solid-state polymerization reaction has converted the molecular cubane precursor into an extended carbon network with long-range order, and there is no evidence of a deviation from the starting elemental composition.

The endogenous polymerization of solid cubane, which largely preserves the initial structural topology, was confirmed through in situ PXRD and infrared spectroscopy. Crystallographic indexing as a function of pressure indicates that the molecular $R\bar{3}$ phase of cubane retains its identity at 25 GPa and shows only the expected contraction of the hexagonal lattice (Figure 1a). After high-pressure heating for 24 h at 250 °C, the X-ray diffraction patterns maintain the same general features, but the Bragg peak of the {101} planes shifts to a lower angle, indicative of a change in the lattice associated with the polymerization reaction (Figure 1b).

Furthermore, the diffraction data on decompression show that the polymerized product exhibits a significantly lower compressibility than molecular cubane (zero-pressure bulk modulus of 14.5 GPa[34]), as shown by the evolution of the d-spacing of the {101} Bragg peak in Figure 1b. This decrease in compressibility also strongly supports the formation of a

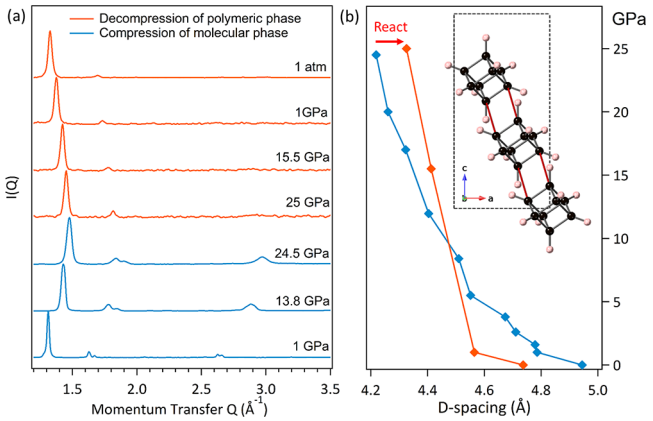

Figure 1. (a) In situ powder X-ray diffraction analysis reveals the structural evolution of cubane during high-pressure synthesis. The blue curves represent PXRD patterns of $R\bar{3}$ cubane upon compression up to 25 GPa. The orange curves represent the PXRD patterns after high-pressure heating and the subsequent decompression. (b) Pressure response of the most intense {101} Bragg peak during the compression of cubane molecules and the decompression of the polymerized product. Inset: crystal structure of $R\bar{3}$ cubane along the [010] direction, which shows the nearest-neighbor molecular stack and the closest intermolecular C···C separation, which is presumably replaced with covalent bonds to create the irreversible lattice distortion.

polymerized extended network with increased structural rigidity. Infrared spectra obtained during polymerization suggest oligomerization of cubane monomers within the starting crystal and further support the topology-preserving polymerization (Figure S2).

The total scattering function $S(Q)$ (Figure 2a) derived from synchrotron X-ray diffraction from a recovered multianvil sample synthesized at 12 GPa reveals sharp Bragg peaks along with broad scattering from an amorphous component. The Bragg peaks index to a trigonal lattice with a = 5.984(2) Å, c = 10.527(5) Å (DICVOL[60] FOM = 161.5), and systematic absences suggest the space group $R\bar{3}$, the same symmetry as molecular cubane, which supports a topology-preserved polymerization reaction. The retention of $R\bar{3}$ symmetry would be remarkable as symmetry preservation after solid-state polymerization is rare.[61] The recovered solid is denser than molecular cubane (lattice parameter a = 6.296 Å, c = 11.735 Å).[62] After the polymerization process, the c-axis decreased by ∼5%, while the a-axis decreased by ∼10%. Given the similarity, it is presumed that the number of atoms per unit cell (C_8H_8, Z = 3) is preserved after polymerization, which gives an estimated density of 1.59 g/cm^3 for the crystalline recovered product (unit volume = 13.6 $Å^3$/CH).

Structural solution of the recovered material via PXRD is challenging as there is only one strong peak and higher-order peaks have extremely low intensities. However, pair distribution function analysis (PDF) is a powerful tool to determine the local atomic environments. The Fourier Transform of the total scattering function S(Q) gives the atomic pair distribution function, $g(r)$, which is related to the reduced pair distribution function, $G(r) = 4\pi\rho_0[1 - g(r)]$, where ρ_0 is the number density of scatterers. Figure 2b shows $G(r)$ for a recovered multianvil sample synthesized at 12 GPa. The first peak at 1.55 Å represents nearest-neighbor carbon-carbon distances and indicates the presence of sp^3 single bonds (dC-$C_{diamond}$ = 1.54 Å). This feature, along with the third neighbor

https://dx.doi.org/10.1021/jacs.9b12352
J. Am. Chem. Soc. 2020, 142, 17944−17955

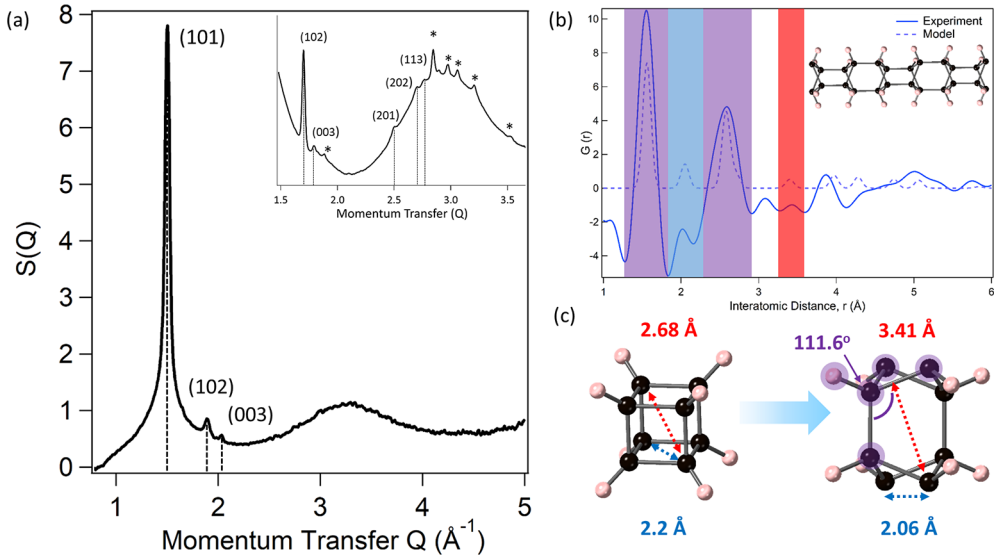

Figure 2. (a) Powder diffraction pattern can be indexed to a hexagonal lattice with lattice parameters a = 5.984(2) Å, c = 10.527(5) Å. The rapid decrease in intensity of higher Q Bragg peaks is consistent with a tubular morphology (see main text). The inset shows a zoom-in view of the total scattering function $S(Q)$. The weak intensities of high Q reflections from the polycubane crystals are indexed and the Bragg peaks assigned to hexagonal boron nitride (the capsule material) are labeled with asterisks. (b) PDF analysis shows tetrahedral carbon connectivity in the local structure, along with characteristic C_8 cages comprising the structural units of the proposed model shown in the inset. The color-coded regions correspond to the carbon-carbon distances in (c). (c) Schematics showing that the C−C−C bond angle has changed from 90° to 111.6°, closer to the tetrahedral angle (109.5°). The original diagonal distance of the square rings (2.2 Å) from starting cubane is downshifted to 2.06 Å, which corresponds to the buckling of the cyclobutane rings in polycubane after strain release.

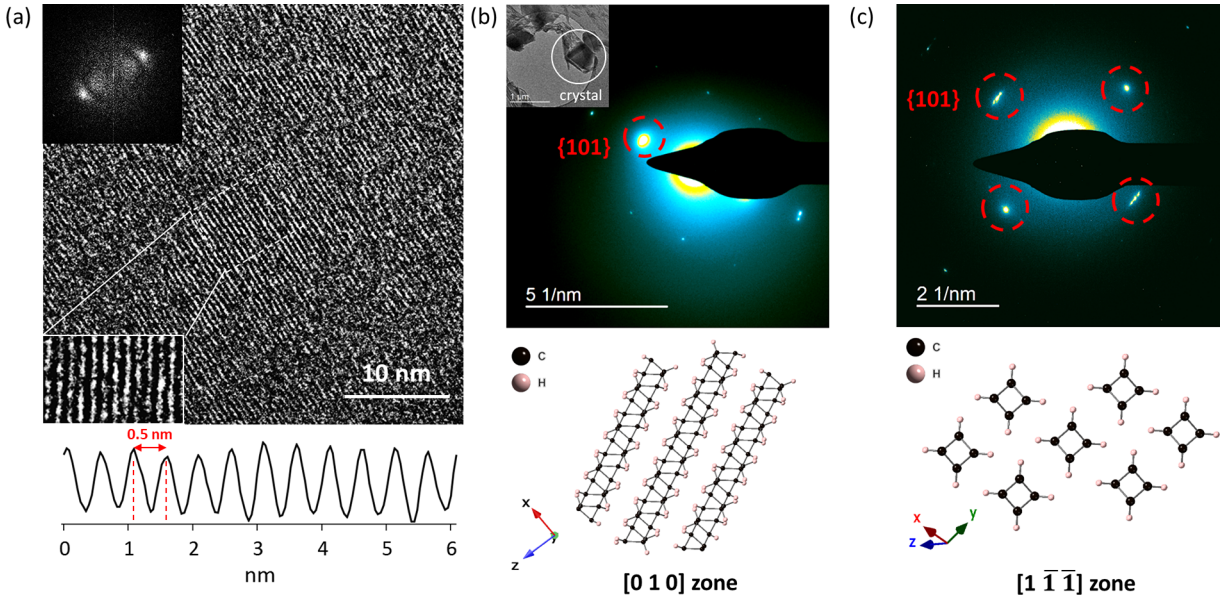

Figure 3. (a) High-resolution imaging with the inset FFT pattern reveals the low-dimensional structure. The arcing in the FFT has a d-spacing of 5 Å, which suggests that the lattice is expanding under electron beam radiation. (b) Selected area electron diffraction of a polycubane crystal viewed along the [010] zone axis with the inset showing the diffracting ∼1 μm single crystal. (c) Diffraction indexed to the [$1\bar{1}1$] zone axis of the hexagonal lattice. The schematics corresponding to each diffraction pattern indicate the orientation of the proposed model structure.

shell located at 2.57 Å (characteristic of a tetrahedral carbon structures with 1:1 C/H stoichiometry[63,64]), clearly shows that a tetrahedral network has been formed. Pristine square cyclobutane rings diagnostic of cubane (2.2 Å) are no longer present in the polymerized material; however, a new peak at 2.0 Å can be assigned to second-neighbor C-C distances across buckled square rings and/or second-neighbor sp^3 C-H distances, which should have low intensity due to the low scattering power of H. In Figure 2c, the structural unit of the proposed polycubane architecture is shown and compared to molecular cubane (structural models are discussed in detail below). The proposed structure may be considered a chain of fused cyclohexane rings (boat conformation) in a back-to-back manner or buckled four-membered rings linked by alternating vertices when viewed down the polymer axis (see Figure 2b inset). Interestingly, these rings are strained and therefore exhibit smaller distances compared to free-standing cyclohexane rings.[64,65] The second nearest-neighbor shell in $G(r)$

https://dx.doi.org/10.1021/jacs.9b12352
J. Am. Chem. Soc. 2020, 142, 17944−17955

located at 2.06 Å and the fifth nearest-neighbor shell located at 3.41 Å can be assigned to the relaxed C_8 cages that comprise the backbone. It is proposed that the transformation driven by the release of ring strain can lead to the observed down-shifting of the second-neighbor shell at 2.0 Å.

Bright-field transmission electron microscopy (TEM) imaging of the sample performed under cryogenic conditions shows long-range parallel striations, which are similar to those observed in benzene nanothreads and other polymeric materials like highly oriented polyacetylene (HOPA; Figure 3a).[66−68] The ∼5 Å spacing between these striations is in agreement with the strong diffraction peak observed by X-rays ($d \approx 4.7$ Å) for {101}. In addition, the azimuthal width of the reflections observed in the corresponding Fast Fourier Transformation (FFT) pattern closely resembles the electron diffraction from carbon nanofibers.[69] The observation of beam-induced lattice dilation suggests the presence of a low-dimensional structure (Figure S3). The {101} planes are presumably associated with the interchain spacings or interlayer spacings of a 1D, or 2D material. Therefore, these van der Waals separations quickly expand upon inelastic collision events which form phonons, free radical species, and secondary electrons that cause heat, branching, and disruption of the crystal lattice.[66,68,70] The corresponding FFT pattern exhibits 2-fold arcs which can be indexed to the {101} reflections. The high-resolution imaging is accompanied by an increase in the mosaicity of the crystal derived from the beam-induced lattice dilation/distortion. This arcing phenomenon is commonly seen in nanothreads and highly oriented polymer samples.[71−73]

The TEM image and the corresponding selected area electron diffraction (SAED) pattern from a ∼1 μm single-crystal of polycubane are shown in Figure 3b. The SAED pattern, which exhibits excellent crystallinity, indexes to a hexagonal lattice along ⟨010⟩ and absences are again in excellent agreement with space group $R\bar{3}$. In Figure 3c, we observe the $\langle 1\bar{1}1 \rangle$ zone of polycubane with the expected angles between the sets of {101} lattice planes being 100° and 80°. Given that $\langle 1\bar{1}1 \rangle$ is perpendicular to ⟨101⟩, the $\langle 1\bar{1}1 \rangle$ zone provides information regarding the end-on packing of the striations observed in Figure 3a. The 4-fold diffraction suggests near-square packing of the constituents, which is also evident across areas of a few hundred nm^2 with direct imaging (Figure S4). In the Fourier-filtered image, the columnar points are arranged in a perfect array with no deviation from the $\langle 1\bar{1}1 \rangle$ axis, which may indicate the near-perfect alignment of straight polymer chains extended across ∼150 nm of sample thickness. When compared with most other carbon-based polymeric materials, it is remarkable to observe a single crystal with full three-dimensional order, as evidenced by the crisp diffraction spots for SAED patterns over two different zones (⟨010⟩ and $\langle 1\bar{1}1 \rangle$). The schematics in Figure 3b,c present the views of the proposed polycubane crystal structure (discussed below) viewed along the [010] and $[1\bar{1}1]$ directions.

In addition to electron diffraction, electron energy loss spectroscopy (EELS) is very useful for determining the bonding in the material. Under cryogenic and ultralow dose conditions (accumulated dose of 24 $e^-/Å^2$), we were able to obtain sufficient signal from a polycubane single crystal with negligible beam damage using a direct electron detector. The C 1s spectrum shows negligible intensity at the 1s to π^* transition (Figure 4). In addition, the π to π^* transition peak is not observed in the low-loss region and further confirms the absence of sp^2 carbon (Figure S5). Here, we provide direct evidence for the formation of a nearly 100% sp^3 extended hydrocarbon material by using a 100% sp^3 carbon precursor. Radiation damage increases the sp^2 carbon content in the sample via fragmentation of C-H bonds very quickly as dose accumulates. Therefore, while higher dose is desired to reveal fine structure, we have to strike a balance between beam damage and signal to probe the pristine bonding environments. Complementary X-ray photoelectron spectroscopy also reveals a purely sp^3-hybridized environment in the local structure of polycubane (Figure S6).

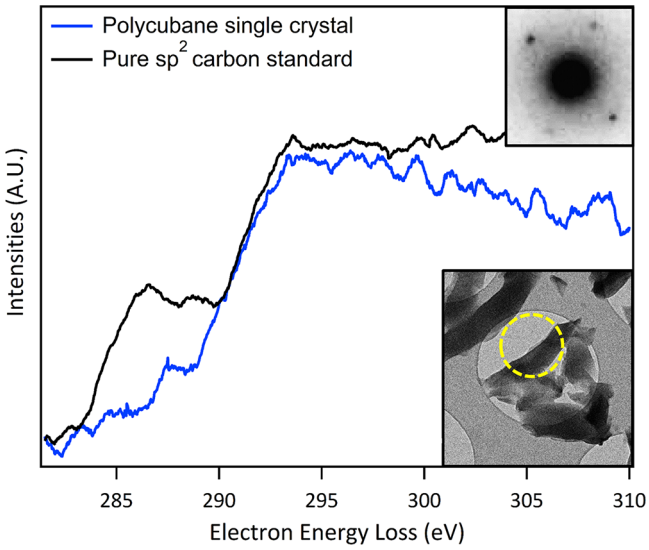

Figure 4. Carbon K-edge Electron Energy Loss Spectroscopy (EELS) analysis of polycubane crystals overlaid with a 100% sp^2 multilayer fullerene standard. The C-K edge spectrum shows that the polycubane crystal is nearly 100% sp^3-hybridized carbon as negligible intensity is observed at 285.0 eV, assigned to the 1s to π^* transition. The inset is a TEM image of the analyzed single crystal and the corresponding selected area diffraction pattern.

Pressure Guides Polycubane Formation. Distinct from conventional pressure-induced polymerization involving the reaction of unsaturated bonds at room temperature, here elevated temperature is also required to drive the reaction. Pressure is clearly important, however, as heating cubane at low pressure results in simple isomerization, what are the specific roles of pressure and temperature during synthesis? We hypothesize that the role of pressure during polymerization is to provide selectivity for specific reaction pathways, while temperature is needed to overcome kinetic barriers. In the simplest model, $\Delta^{\ddagger}V$ is a function of pressure and it approaches zero as pressure increases because there's simply not much room for atoms to move in an extremely compressed system.[32] Therefore, the prearranged monomers can polymerize cleanly if they are held in alignment in the solid state within van der Waals distances appropriate for a diradical chain reaction. Otherwise, the thermally activated reaction would produce a mixture of cubane isomers/branched oligomers, ultimately creating a disorder material. In fact, the intramolecular electron transfer process for cubyl radicals is highly unfavorable;[74] thus, the unpaired spin radicals are either trapped and form neutral localized "solitons" on the backbone or they form a covalent bond with the neighboring cubyl radicals. It is presumed that these solitons could contribute to the EPR signal observed in

https://dx.doi.org/10.1021/jacs.9b12352
J. Am. Chem. Soc. 2020, 142, 17944−17955

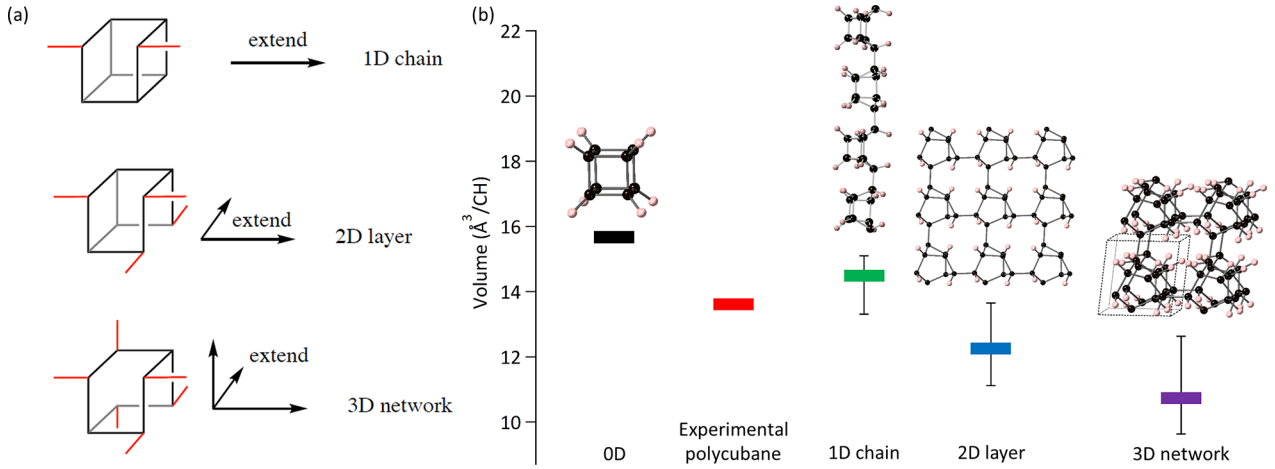

Figure 5. Novel extended hydrocarbon scaffolds constructed through molecular architecture of cubane. (a) Proposed mechanism for the formation of cubane-derived 1D chain, 2D layer, and 3D network. (b) Comparison of the unit volume of the polymerized product observed in experiments and the modeled cubane-derived scaffolds where the covalent connectivity extends in one, two, and three dimensions, which reveals the low-dimensional nature of polycubane formed in high-pressure reactions. Black bars indicates the volume ranges for various CH models.

the experimental spectrum of the recovered product (Figure S7).[74]

A series of synthesis experiments conducted at various pressures from 2 to 30 GPa confirm the hypothesis that pressure constrains reaction pathways. As shown in Figure S7, the total scattering functions $S(Q)$ of the DAC samples synthesized at pressure above 25 GPa show good crystallinity (i.e., sharp, intense Bragg peaks). The samples made at 12 GPa exhibit reduced crystallinity while the Bragg peaks are still clear, indicating that the extent of crystallinity diminishes with decreasing pressure. Further reducing the synthesis pressure to 2−4 GPa results in samples with limited long-range order. Interestingly, the {101} Bragg peak shows a systematic shift to lower Q with decreasing pressure. This shift, together with broadened peaks, suggests that alternative reaction pathways are enabled at lower pressure. Without the guidance of high pressure/uniaxial stress, thermally activated cubyl radicals can pursue multiple pathways, which may result in shorter, kinked chains, accompanied by loose packing to accommodate end-group conformations (Figure S8).

Polymerization Pathways and Cubane-Derived Scaffolds. We now explore potential solid-state polymerization pathways for molecular cubane and discuss the proposed polycubane structural model along with other possible cubane-derived scaffolds. The molecular $R\bar{3}$ phase hosts three equivalent nearest-neighbor stacks of molecules along the $\langle 1\bar{1}1\rangle$, $\langle 211\rangle$, and $\langle 12\bar{1}\rangle$ directions in the hexagonal lattice along which polymerization is most likely to occur. Cubane is a molecule with cubic symmetry (O_h) and possesses three sets of orthogonal square rings. Cleaving one bond on a square ring will produce two radicals that could propagate and linearly extend the covalent bonding along one-dimensional chains (Figure 5a). Breaking two orthogonal bonds per cube could extend the connectivity into two-dimensional layers. Similarly, breaking and interlinking three orthogonal bond directions produces a three-dimensional network. Figure 5b shows how such hypothetical polymers are formed from the starting $R\bar{3}$ phase. We emphasize that the density of the CH scaffolds increases with dimensionality, which is attributed to the replacement of van der Waals distances with covalent bonding. The unit volume of the recovered crystal therefore becomes important for determining the dimensionality of the product (Figure 5b). The simplest 1D chains (with one bond between cubes) exhibit the largest unit volume (~14.5 Å^3/CH), greater than 2D layers (~12.25 Å^3/CH) and 3D frameworks (~10.7 Å^3/CH). In fact, solid molecular cubane has an exceptionally high density (1.29 g/cm^3, 16.8 Å^3/CH) as compared to other hydrocarbons such as adamantane (1.09g/cm^3) and polyacetylene (1.17g/cm^3).[62] These hypothetical cubane-derived polymers are dense extended solids with rigid sp^3 bonding, distinct from COFs[11] and π-conjugated macrocycles.[75]

The experimental volume of 13.6 Å^3/CH, intermediate to single-bonded chains and 2D sheets, suggests a low-dimensional structure that retains some van der Waals spacings. While cubane chains with only one bond between monomers exhibit a larger volume than experiment, a series of multiply bonded cubane-derived carbon tubes exhibit much better agreement. A family of 1D structures can be constructed by enumerating bonding between the different cube positions (1, 2, 3, and 4) of adjacent faces within a molecular stack. These 1D structures with two bonds between monomers exhibit a volume range similar to experiment as indicated in Figure 5b. In particular, "Cub-13" is 13.2 Å^3/CH. This tubular architecture, constructed from face-aligned cubes with bonds that propagate in opposite directions from alternating vertices (i.e., 2,2-meta-polycubane), can be considered one of the smallest-diameter members within the family of carbon nanothreads. This Cub-13 model was used in the interpretation of the PDF and SAED data above. More details about enumerated 1D structures are presented in Figure S9.

It is also important to compare the experimental results with other possible CH polymorphs. Several CH structures have been proposed to be thermodynamically stable or metastable and could potentially be obtained from the compression of small CH molecules.[10,76] For example, several proposed graphane structures exhibit volumes from 11.12 to 13.65 Å^3/CH depending on stacking geometry.[77] Benzene polymer II[10] possesses a volume of 12.8 Å^3/CH, and the hypothetical 3D polymorphs K_4-CH,[78] hex-CH,[79] and R_6-CH[80] all have volumes near 9.65 Å^3/CH. Interestingly, we found that the 3D polymer Cub-3D, composed of building blocks similar to [2,2,2]bicyclooctane, has a higher volume (10.7 Å^3/CH) and is the lowest-energy structure among all of the hypothetical cubane-derived polymers we enumerated. Figure S9 provides a

https://dx.doi.org/10.1021/jacs.9b12352
J. Am. Chem. Soc. 2020, 142, 17944−17955

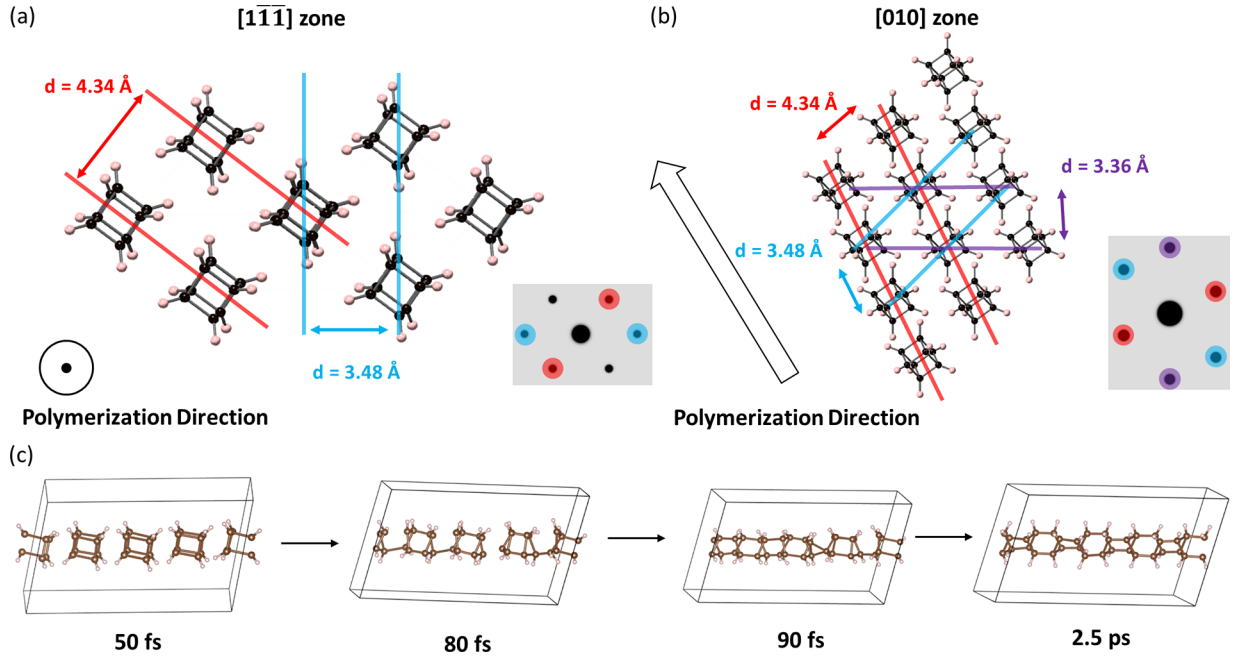

Figure 6. Hexagonal cubane precursor crystal viewed from (a) the [1$\bar{1}\bar{1}$] zone axis and (b) the [010] axis, showing diffraction planes and their interplanar spacings at 24.9 GPa with the orientation and simulated diffraction spots (inset). Once initiated, the polymerization propagates along the ⟨$\bar{1}$11⟩ direction, which becomes the end-on view of the polymer array after the topology-preserved reaction. (c) Molecular dynamics simulation shows that the diradical polymerization of cubane occurs spontaneously under uniaxial stress of 30 GPa. In the simulation, the reaction propagates along three equivalent crystallographic directions, which are [$\bar{1}$11], [211], and [$\bar{1}$21], in good agreement with experimental observations.

detailed comparison of the heats of formation for cubane-derived polymers. All of the proposed cubane-derived polymers and other CH polymorphs have lower total energy than molecular cubane (due largely to the release of stain energy), providing energetic driving force for their formation.[78] While most 3D structures exhibit too small of a volume compared with experiment, low-density diamond monohydride (DMH) exhibits a volume near 12.7 Å^3/CH and shows some consistency with the local structure based on PDF analysis.[81] This higher unit volume is natural because these DMH structures are constructed by punching holes in an ideal diamond lattice and "healing" the dangling bonds with hydrogen.[81] It is noted that a modified version of a DMH-type structure, which can be viewed as interconnected chains, could potentially agree with the experimental data, although there is no clear reaction pathway to it from the molecular cubane structure. Despite agreement with some XRD features, most alternative CH polymorphs are not consistent with experimental observations of crystal lattice and symmetry, which is well constrained from XRD, SAED, and high-resolution electron microscopy. Detailed comparisons with other models are summarized in Table S9. In general, the formation of noncubane derived CH materials from cubane would require a drastic change in bonding topology, which is unlikely based on in situ X-ray and IR studies. Therefore, cubane-derived architectures represent the most plausible structural candidates for the recovered crystalline material.

Overall, the Cub-13 nanothread model shows the best agreement with experimental data. The relative diffraction peak intensities are consistent with a cylindrical form factor, similar to benzene-derived nanothreads as well as other one-dimensional materials such as carbon and vanadium oxide nanotubes.[82,83] Theoretical layered graphane structures could give a similar diffraction pattern and some show similar local structures (see Figure S10). Note that hydrogen atoms were not taken into consideration in the PDF calculations, due to their weak scattering power.[84] However, again, straightforward topological pathways from cubane to graphane do not appear to exist and are unlikely based on crystal lattice and symmetry (Table S9). We note, however, a deficiency of the Cub-13 nanothread model is that the final DFT-optimized structure shows some deviation from the XRD and SAED experiments. The DFT-relaxed model shows a distortion from the experimentally observed hexagonal symmetry with a = 5.953 Å, b = 5.954 Å, c = 10.114 Å, α = 99.57°, β = 80.2°, γ = 115.46° (see the Supporting Information for a structural model). Modified versions of this basic structural model with alternate bonding sequences along the backbone and inter-registry packing could lead to a range of structural variants (see Table S9 and Figure S11).

To gain further insight into the reaction mechanism of dense solid cubane, we performed metadynamics simulations[57] at 10 GPa and 500 K. Metadynamics is a powerful technique to improve the sampling of a system where ergodicity is hindered by kinetic barriers. Initial polymerization was generally observed to occur within the first 200 metasteps of the run along the nearest-neighbor stack of molecules. Experimentally, cubane remains stable[34] down to C···C van der Waals contact distances that are broadly characteristic of intermolecular reactions for unsaturated molecules such as benzene, including lattice phonon effects.[85] Simulations of the reaction mechanism thus reflect the importance of thermal excitation over a reaction barrier against bond cleavage in the saturated cubane system. The reaction should most easily propagate along this direction, and the relaxed structures show one-dimensional polycubane chains with one bond between the vertices of nearest neighbors (Figure S12). This polymerization could proceed along any of the equivalent stack directions, for

https://dx.doi.org/10.1021/jacs.9b12352
J. Am. Chem. Soc. 2020, 142, 17944−17955

example, ⟨1$\bar{1}$1⟩ (Figure 6a,b). The uniaxial stress component of the applied pressure may potentially differentiate nominally equivalent molecular stacks and guide the polymerization along a certain direction, similar to the mechanochemical synthesis of benzene nanothreads.[30]

First-principles molecular dynamics (MD) simulations were performed to examine the influence of uniaxial stress and to explore the possibility of forming additional bonds between molecular units. Figure 6c shows structural snapshots at several key steps during a MD simulation performed at 500 K with uniaxial stress of 30 GPa applied along the nearest-neighbor ⟨1$\bar{1}$1⟩ direction. As shown in the snapshots, the stacks spontaneously polymerize along the uniaxial stress direction to form sp^3-bonded carbon tubes (Figure S13) in the Cub-13 structure, identical to that found through structural enumeration. The influence of uniaxial stress was also observed experimentally by comparing DAC and multianvil samples. DAC samples, which possess larger uniaxial stress, always exhibit higher crystallinity and sharper XRD linewidths than multianvil samples, even at the same nominal synthesis conditions (Figure S14). While the Cub-13 structure was observed directly in MD simulations, several other 1D structures could potentially form though different reaction pathways (Figure S9) as mentioned above. 1D polycubane chains could further react to produce higher-dimensional networks, (Figure S15). However, we did not observe a tendency toward 2D or 3D structures in the metadynamics and MD simulations. Cubane molecules in MD simulations performed under hydrostatic conditions did not polymerize at pressures as high as 60 GPa. To further probe the reaction mechanism, we calculated the lowest-energy reaction pathways using the Pallas method.[86] We find that the lowest-energy pathway at 25 GPa reflects the same mechanism observed in our MD simulations with a barrier of 34 kcal/mol (Figure S16).

The 1D structure predicted by MD simulations and structural enumeration is also supported by the TEM results. If this model is an accurate description of the crystal structure, then ordered cubane nanothreads can be clearly observed on the ⟨010⟩ zone. Given the exceptional ordering observed in HRTEM images and the sharp reflections from SAED (Figure 3, cf. benzene nanothreads[66]), it is possible that these threads possess identical orientations within the array and crystallize with axial registry. Additionally, the rapid decrease of diffraction intensity out to fifth order is also consistent with a cylindrical form factor. A comparison of the form factors for tubular and layered materials is summarized in Figure S17 and Table S17. These TEM observations suggest that the topology-preserved radical polymerization process creates an array of rigid, rod-shape threads with consistent axial alignment and minimal angular orientational disorder. The beam-induced isotropic lattice expansion observed in the corresponding FFT patterns of the HREM images also supports the indexing of the end-on view along the ⟨1$\bar{1}$1⟩ direction and the 1D nature of the material. The calculated thread axes are only 4.9 Å apart in the model nanothread array, which is in close agreement with HRTEM images.

As opposed to packing into a two-dimensional pseudohexagonal unit cell as observed in the benzene and pyridine nanothreads, cubane nanothreads adopt a lower-symmetry packing. Calculations show that the van der Waals cohesive force of cubane threads (Cub-13) spontaneously drives a square array of randomly oriented nanothreads into an ordered packing which gives crystallographic angles of 78° and 102° (Figure S18), close to the experimentally observed pattern viewed along the ⟨1$\bar{1}$1⟩ axis. The driving force that leads to the near-square packing could be the inherent 4-fold symmetry of each individual thread and the ABAB staggered conformation of the Cub-13 nanothread model. This efficient packing may contribute the high hardness and elasticity (Figure S19). An orientationally ordered packing of thiophene-derived nanothreads that arises from an anisotropic azimuthal orientation was recently reported.[29] Paradoxically, these low-symmetry packings signal a higher degree of structural order in the nanothread arrays.[29]

Among all of the potential hydrocarbon structures examined, the Cub-13 nanothread model provides the best agreement with experiments, and its spontaneous formation and subsequent crystal packing were observed in MD simulations. While we cannot fully exclude the possibility for other structure types, the experimental observations combined with simulation results provide strong support for a 1D nanothread material, with potentially interesting mechanical properties. One-dimensional carbon nanomaterials are of continuing interest for their exceptional strength and stiffness. In the present case, the sp^3 cubane nanothreads possess a rigid, cage-like backbone over an extremely small thickness (~0.2 nm), which should result in exceedingly large stiffness. The tensile stiffness of one-dimensional systems largely depends on how axial extension is accommodated by bond bending and bond stretching. For example, carbyne polymer, which is a hypothetical 1-D carbon nanomaterial, has ultrahigh tensile stiffness (3.46 TPa estimated with a linear density model) since 100% of the axial extension must be accounted for by bond stretching.[17,88] On the other hand, a single-wall carbon nanotube was calculated to possess a Young's modulus of ~1 TPa.[89]

Table 1 compares calculated Young's moduli for various nanothread structures using the linear atom density method, which has been used widely to quantify the stiffness of nanothreads and nanowires.[17,87,90] Within this method, the

Table 1. Comparisons of the Tensile Stiffness between Cubane Nanothread and Enumerated sp^3 Nanothread Structures Derived from Benzene

structure	Young's modulus (TPa)	1D Young's modulus (10^{-8} N)	cross-sectional area (Å^2)[a]
cubane nanothread (Cub-13)	1.19	12.69	10.7
achiral benzene threads			
(3,0) tube (123456)	1.16	18.32	15.8
polymer I (135462)	0.98	13.47	13.8
square (143562)	0.93	12.64	13.6
5−8 (135462)	0.90	13.36	14.8
polymer I' (153624)	0.59	8.76	14.9
zipper (143562)	1.08	15.05	13.9
stiff, chiral benzene threads			
polytwistane (143652)	1.11	15.52	14.0
stiff chiral 2 (136254)	0.73	11.50	15.8
siff chiral 3 (136425)	0.64	9.56	14.9
stiff chiral 4 (135462)	0.63	9.48	15.0

[a]The cross-sectional area is calculated by $A = \lambda V_0$, where λ is linear carbon atom density and V_0 is unit volume per sp^3 carbon atom in diamond lattice (5.705 Å^3).[87]

https://dx.doi.org/10.1021/jacs.9b12352
J. Am. Chem. Soc. 2020, 142, 17944−17955

cross-sectional area term (A) in the definition of Young's modulus is replaced with λV_0, where the reference volume V_0 is the volume per sp^3 carbon in bulk diamond (5.705 Å^3/C). The linear carbon density (λ) is defined as the number of carbon atoms (n_c) per unstrained unit length (L_0). Using this methodology, the Young's modulus (Y) and spring constant (k_0) for cubane can be directly compared to the values enumerated for benzene thread structures.[87] An alternative method used to characterize the stiffness is the "1-D Young's modulus".[91] Results from this method are expressed in 1-D stress (force) to avoid the ambiguous definition of a nanothread diameter. Interestingly, we observe that the stiffest benzene thread structures, such as polytwistane (143652) and tube (3,0) (123456), have a higher 1-D Young's modulus than the cubane nanothread. However, when the cross-sectional area is taken into account through the linear density method, the cubane thread exhibits superior tensile stiffness (1.19 TPa), even higher than tube (3,0), which is consistent with our expectation for the ultrathin thread. Cubane-derived nanothreads are thus a new 1-D sp^3 material that represents one of the stiffest 1-D materials known.

CONCLUSION

We have demonstrated that a crystalline nearly 100% sp^3-bonded extended carbon solid can be produced by the thermally activated solid-state polymerization of the highly strained and saturated cubane molecule. Molecular dynamics simulations are in agreement with the experimental results that a one-dimensional radical polymerization reaction can be guided by the uniaxial stress component of the applied pressure to produce a new diamond nanothread architecture. We suggest that the solid-state polymerization route described here may be applied to other classes of strained, saturated monomers, and that the combination of temperature (to overcome barriers) with pressure (to enhance pathway selectivity) offers new avenues for exploration for the synthesis of extended solid materials. The introduction of nanoarchitecture through strained molecules provides access to the kinetically controlled synthesis of materials with enhanced control through various P-T conditions. Among all of the theoretical structural candidates, the predicted cubane nanothread structure has an extremely small thickness (~0.2 nm) and represents one of the smallest possible nanothreads with calculated stiffness comparable to the most rigid structures known.

ASSOCIATED CONTENT

Supporting Information

The Supporting Information is available free of charge at https://pubs.acs.org/doi/10.1021/jacs.9b12352.

Materials and methods, modeling and simulations, additional discussion, supporting figures (PDF)
Additional structrual model (CIF)

AUTHOR INFORMATION

Corresponding Authors

Haw-Tyng Huang − *Department of Materials Science and Engineering, The Pennsylvania State University, University Park, Pennsylvania 16802, United States;* orcid.org/0000-0002-9953-1623; Email: haw-tyng.huang@stonybrook.edu

Timothy A. Strobel − *Geophysical Laboratory, Carnegie Institution for Science, Washington, DC 20015, United States;* orcid.org/0000-0003-0338-4380; Email: tstrobel@carnegiescience.edu

Authors

Li Zhu − *Geophysical Laboratory, Carnegie Institution for Science, Washington, DC 20015, United States;* orcid.org/0000-0001-8588-9379

Matthew D. Ward − *Geophysical Laboratory, Carnegie Institution for Science, Washington, DC 20015, United States*

Tao Wang − *Department of Physics, The Pennsylvania State University, University Park, Pennsylvania 16802, United States;* orcid.org/0000-0003-2833-1592

Bo Chen − *Department of Chemistry, The Pennsylvania State University, University Park, Pennsylvania 16802, United States;* orcid.org/0000-0002-5084-1321

Brian L. Chaloux − *Chemistry Division, U.S. Naval Research Laboratory, Washington, DC 20375, United States;* orcid.org/0000-0003-0366-2280

Qianqian Wang − *Geophysical Laboratory, Carnegie Institution for Science, Washington, DC 20015, United States*

Arani Biswas − *Department of Chemistry, The Pennsylvania State University, University Park, Pennsylvania 16802, United States;* orcid.org/0000-0002-5659-7171

Jennifer L. Gray − *Materials Research Institute, The Pennsylvania State University, University Park, Pennsylvania 16802, United States*

Brooke Kuei − *Department of Materials Science and Engineering, The Pennsylvania State University, University Park, Pennsylvania 16802, United States*

George D. Cody − *Geophysical Laboratory, Carnegie Institution for Science, Washington, DC 20015, United States*

Albert Epshteyn − *Chemistry Division, U.S. Naval Research Laboratory, Washington, DC 20375, United States;* orcid.org/0000-0002-4489-2296

Vincent H. Crespi − *Department of Materials Science and Engineering, Department of Chemistry, Department of Physics, and Materials Research Institute, The Pennsylvania State University, University Park, Pennsylvania 16802, United States*

◇**John V. Badding** − *Department of Materials Science and Engineering, Department of Chemistry, Department of Physics, and Materials Research Institute, The Pennsylvania State University, University Park, Pennsylvania 16802, United States;* orcid.org/0000-0002-4517-830X

Complete contact information is available at: https://pubs.acs.org/10.1021/jacs.9b12352

Notes

The authors declare no competing financial interest.
◇Deceased.

ACKNOWLEDGMENTS

We thank M. Amsler, X. Li, and S. Juhl for valuable discussion and assistance for this work. We acknowledge M. Hazen and J. Abrahamson for advice and assistance for TEM sample preparation and thank Y. Fei for access to the multianvil facilities. We also thank V. Prakapenka, O. Borkiewicz, and C. Kenney-Benson for help with synchrotron X-ray experiments. This work was supported by DARPA under ARO Contract No. W31P4Q-13-I-0005 with additional support from the U.S. Army Research Office under Grant No. W911NF-17-1-0604. We also acknowledge support from the Energy Frontier Research in Extreme Environments (EFree) Center, funded by the U.S. Department of Energy, Office of Science (award

number DE-SC0001057) for supporting portions of the TEM work. A portion of the computational investigation by TW, BC, and VHC was supported by the Center for Nanothread Chemistry, an NSF Center for Chemical Innovation (CHE-1832471). Portions of this work were performed at HPCAT (Sector 16), GSECARS (The University of Chicago, sector 13), and XSD-SRS (X-ray Science Division, sector 11), Advanced Photon Source (APS), Argonne National Laboratory. HPCAT operations are supported by the DOE-NNSA's Office of Experimental Sciences. GeoSoilEnviroCARS is supported by the National Science Foundation−Earth Sciences (EAR-1634415) and Department of Energy-GeoSciences (DE-FG02-94ER14466). This research used resources of the Advanced Photon Source, a U.S. Department of Energy (DOE) Office of Science User Facility operated for the DOE Office of Science by Argonne National Laboratory under Contract No. DE-AC02-06CH11357. B.C. acknowledges the computing resource provided by the Extreme Science and Engineering Discovery Environment (XSEDE) Comet cluster at the San Diego Supercomputer Center through allocation CHE180059.

REFERENCES

(1) Hoffmann, R.; Hughbanks, T.; Kertesz, M.; Bird, P. H. Hypothetical Metallic Allotrope of Carbon. *J. Am. Chem. Soc.* **1983**, *105*, 4831−4832.
(2) Itoh, M.; Kotani, M.; Naito, H.; Sunada, T.; Kawazoe, Y.; Adschiri, T. New Metallic Carbon Crystal. *Phys. Rev. Lett.* **2009**, *102*, 55703.
(3) Blase, X.; Gillet, P.; San Miguel, A.; Mélinon, P. Exceptional Ideal Strength of Carbon Clathrates. *Phys. Rev. Lett.* **2004**, *92*, 215505.
(4) Németh, P.; Garvie, L. A. J.; Aoki, T.; Dubrovinskaia, N.; Dubrovinsky, L.; Buseck, P. R. Lonsdaleite Is Faulted and Twinned Cubic Diamond and Does Not Exist as a Discrete Material. *Nat. Commun.* **2014**, *5*, 5447.
(5) Shiell, T. B.; McCulloch, D. G.; Bradby, J. E.; Haberl, B.; Boehler, R.; McKenzie, D. R. Nanocrystalline Hexagonal Diamond Formed from Glassy Carbon. *Sci. Rep.* **2016**, *6*, 37232.
(6) Wang, Y.; Dong, X.; Tang, X.; Zheng, H.; Li, K.; Lin, X.; Fang, L.; Sun, G.; Chen, X.; Xie, L.; Bull, C. L.; Funnell, N. P.; Hattori, T.; Sano-Furukawa, A.; Chen, J.; Hensley, D. K.; Cody, G.; Ren, Y.; Lee, H. H.; Mao, H.-K. Pressure-Induced Diels-Alder Reactions in C6H6-C6F6 Cocrystal towards Graphane Structure. *Angew. Chem., Int. Ed.* **2019**, *58*, 1468−1473.
(7) Kondrin, M. V; Nikolaev, N. A.; Boldyrev, K. N.; Shulga, Y. M.; Zibrov, I. P.; Brazhkin, V. V. Bulk Graphanes Synthesized from Benzene and Pyridine. *CrystEngComm* **2017**, *19*, 958−966.
(8) Ward, M. D.; Huang, H.-T.; Zhu, L.; Biswas, A.; Popov, D.; Badding, J. V.; Strobel, T. A. Chemistry through Cocrystals: Pressure-Induced Polymerization of C2H2·C6H6 to an Extended Crystalline Hydrocarbon. *Phys. Chem. Chem. Phys.* **2018**, *20*, 7282−7294.
(9) Lian, C.-S.; Wang, J.-T.; Duan, W.; Chen, C. Phonon-Mediated High-Tcsuperconductivity in Hole-Doped Diamond-like Crystalline Hydrocarbon. *Sci. Rep.* **2017**, *7*, 1464.
(10) Wen, X.-D.; Hoffmann, R.; Ashcroft, N. W. Benzene under High Pressure: A Story of Molecular Crystals Transforming to Saturated Networks, with a Possible Intermediate Metallic Phase. *J. Am. Chem. Soc.* **2011**, *133*, 9023−9035.
(11) Diercks, C. S.; Yaghi, O. M. The Atom, the Molecule, and the Covalent Organic Framework. *Science* **2017**, *355*, eaal1585.
(12) Côté, A. P.; Benin, A. I.; Ockwig, N. W.; Keeffe, M.; Matzger, A. J.; Yaghi, O. M. Porous, Crystalline, Covalent Organic Frameworks. *Science* **2005**, *310*, 1166−1170.
(13) Hemley, R. J. Effects of High Pressure on Molecules. *Annu. Rev. Phys. Chem.* **2000**, *51*, 763−800.
(14) McMillan, P. F. New Materials from High-Pressure Experiments. *Nat. Mater.* **2002**, *1*, 19.
(15) Brazhkin, V. V; Lyapin, A. G.; Hemley, R. J. Harder than Diamond: Dreams and Reality. *Philos. Mag. A* **2002**, *82*, 231−253.
(16) Mao, W. L.; Mao, H.-K.; Eng, P. J.; Trainor, T. P.; Newville, M.; Kao, C.; Heinz, D. L.; Shu, J.; Meng, Y.; Hemley, R. J. Bonding Changes in Compressed Superhard Graphite. *Science* **2003**, *302*, 425−427.
(17) Stojkovic, D.; Zhang, P.; Crespi, V. H. Smallest Nanotube: Breaking the Symmetry of sp3 Bonds in Tubular Geometries. *Phys. Rev. Lett.* **2001**, *87*, 125502.
(18) Barua, S. R.; Quanz, H.; Olbrich, M.; Schreiner, P. R.; Trauner, D.; Allen, W. D. Polytwistane. *Chem. - Eur. J.* **2014**, *20*, 1638−1645.
(19) Fitzgibbons, T. C.; Guthrie, M.; Xu, E.; Crespi, V. H.; Davidowski, S. K.; Cody, G. D.; Alem, N.; Badding, J. V. Benzene-Derived Carbon Nanothreads. *Nat. Mater.* **2015**, *14*, 43−47.
(20) Ward, M. D.; Tang, W. S.; Zhu, L.; Popov, D.; Cody, G. D.; Strobel, T. A. Controlled Single-Crystalline Polymerization of C10H8·C10F8 under Pressure. *Macromolecules* **2019**, *52*, 7557−7563.
(21) Li, X.; Wang, T.; Duan, P.; Baldini, M.; Huang, H.-T.; Chen, B.; Juhl, S. J.; Koeplinger, D.; Crespi, V. H.; Schmidt-Rohr, K.; Hoffmann, R.; Alem, N.; Guthrie, M.; Zhang, X.; Badding, J. V. Carbon Nitride Nanothread Crystals Derived from Pyridine. *J. Am. Chem. Soc.* **2018**, *140*, 4969−4972.
(22) Nobrega, M. M.; Teixeira-Neto, E.; Cairns, A. B.; Temperini, M. L. A.; Bini, R. One-Dimensional Diamondoid Polyaniline-like Nanothreads from Compressed Crystal Aniline. *Chem. Sci.* **2018**, *9*, 254−260.
(23) Zhan, H.; Zhang, G.; Tan, V. B. C.; Cheng, Y.; Bell, J. M.; Zhang, Y.-W.; Gu, Y. From Brittle to Ductile: A Structure Dependent Ductility of Diamond Nanothread. *Nanoscale* **2016**, *8*, 11177−11184.
(24) Roman, R. E.; Kwan, K.; Cranford, S. W. Mechanical Properties and Defect Sensitivity of Diamond Nanothreads. *Nano Lett.* **2015**, *15*, 1585−1590.
(25) Silveira, J. F. R. V; Muniz, A. R. First-Principles Calculation of the Mechanical Properties of Diamond Nanothreads. *Carbon* **2017**, *113*, 260−265.
(26) Zhan, H.; Gu, Y. Thermal Conductivity of Diamond Nanothread. *Micro and Nano Technologies*; Elsevier: Amsterdam, 2017; Chapter 7, pp 185−204.
(27) Zhan, H.; Zhang, G.; Zhang, Y.; Tan, V. B. C.; Bell, J. M.; Gu, Y. Thermal Conductivity of a New Carbon Nanotube Analog: The Diamond Nanothread. *Carbon* **2016**, *98*, 232−237.
(28) Zhu, T.; Ertekin, E. Phonons, Localization, and Thermal Conductivity of Diamond Nanothreads and Amorphous Graphene. *Nano Lett.* **2016**, *16*, 4763−4772.
(29) Biswas, A.; Ward, M. D.; Wang, T.; Zhu, L.; Huang, H.-T.; Badding, J. V; Crespi, V. H.; Strobel, T. A. Evidence for Orientational Order in Nanothreads Derived from Thiophene. *J. Phys. Chem. Lett.* **2019**, *10*, 7164−7171.
(30) Li, X.; Baldini, M.; Wang, T.; Chen, B.; Xu, E.; Vermilyea, B.; Crespi, V. H.; Hoffmann, R.; Molaison, J. J.; Tulk, C. A.; Guthrie, M.; Sinogeikin, S; Badding, J. V. Mechanochemical Synthesis of Carbon Nanothread Single Crystals. *J. Am. Chem. Soc.* **2017**, *139*, 16343−16349.
(31) Duan, P.; Li, X.; Wang, T.; Chen, B.; Juhl, S. J.; Koeplinger, D.; Crespi, V. H.; Badding, J. V.; Schmidt-Rohr, K. The Chemical Structure of Carbon Nanothreads Analyzed by Advanced Solid-State NMR. *J. Am. Chem. Soc.* **2018**, *140*, 7658−7666.
(32) Chen, B.; Hoffmann, R.; Cammi, R. The Effect of Pressure on Organic Reactions in Fluids-a New Theoretical Perspective. *Angew. Chem., Int. Ed.* **2017**, *56*, 11126−11142.
(33) Yang, F.; Lin, Y.; Baldini, M.; Dahl, J. E. P.; Carlson, R. M. K.; Mao, W. L. Effects of Molecular Geometry on the Properties of Compressed Diamondoid Crystals. *J. Phys. Chem. Lett.* **2016**, *7*, 4641−4647.
(34) Huang, H.-T.; Zhu, L.; Ward, M. D.; Chaloux, B. L.; Hrubiak, R.; Epshteyn, A.; Badding, J. V; Strobel, T. A. Surprising Stability of Cubane under Extreme Pressure. *J. Phys. Chem. Lett.* **2018**, *9*, 2031−2037.

https://dx.doi.org/10.1021/jacs.9b12352
J. Am. Chem. Soc. 2020, 142, 17944−17955

(35) Matsuoka, S.; Ogiwara, N.; Ishizone, T. Formation of Alternating Copolymers via Spontaneous Copolymerization of 1,3-Dehydroadamantane with Electron-Deficient Vinyl Monomers. *J. Am. Chem. Soc.* **2006**, *128*, 8708−8709.
(36) Kaszynski, P.; Michl, J. [N]Staffanes: A Molecular-Size "Tinkertoy" Construction Set for Nanotechnology. Preparation of End-Functionalized Telomers and a Polymer of [1.1.1]Propellane. *J. Am. Chem. Soc.* **1988**, *110*, 5225−5226.
(37) Wu, W.; Gu, J.; Song, J.; Shaik, S.; Hiberty, P. C. The Inverted Bond in [1.1.1]Propellane Is a Charge-Shift Bond. *Angew. Chem.* **2009**, *121*, 1435−1438.
(38) Marutheeswaran, S.; Jemmis, E. D. Adamantane-Derived Carbon Nanothreads: High Structural Stability and Mechanical Strength. *J. Phys. Chem. C* **2018**, *122*, 7945−7950.
(39) Eaton, P. E. Cubanes: Starting Materials for the Chemistry of the 1990s and the New Century. *Angew. Chem., Int. Ed. Engl.* **1992**, *31*, 1421−1436.
(40) Gilardi, R.; Maggini, M.; Eaton, P. E. X-Ray Structures of Cubylcubane and 2-Tert-Butylcubylcubane: Short Cage-Cage Bonds. *J. Am. Chem. Soc.* **1988**, *110*, 7232−7234.
(41) Macreadie, L. K.; Mensforth, E. J.; Babarao, R.; Konstas, K.; Telfer, S. G.; Doherty, C. M.; Tsanaktsidis, J.; Batten, S. R.; Hill, M. R. CUB-5: A Contoured Aliphatic Pore Environment in a Cubic Framework with Potential for Benzene Separation Applications. *J. Am. Chem. Soc.* **2019**, *141*, 3828−3832.
(42) Eaton, P. E.; Nordari, N.; Tsanaktsidis, J.; Upadhyaya, S. P. Barton Decarboxylation of Cubane-1,4-Dicarboxylic Acid: Optimized Procedures for Cubanecarboxylic Acid and Cubane. *Synthesis* **1995**, *1995*, 501.
(43) Ko, E. J.; Savage, G. P.; Williams, C. M.; Tsanaktsidis, J. Reducing the Cost, Smell, and Toxicity of the Barton Reductive Decarboxylation: Chloroform as the Hydrogen Atom Source. *Org. Lett.* **2011**, *13*, 1944−1947.
(44) Mao, H. -K.; Xu, J.; Bell, P. M. Calibration of the Ruby Pressure Gauge to 800 Kbar under Quasi-Hydrostatic Conditions. *J. Geophys. Res.* **1986**, *91*, 4673−4676.
(45) Heinz, D. L.; Jeanloz, R. The Equation of State of the Gold Calibration Standard. *J. Appl. Phys.* **1984**, *55*, 885−893.
(46) Hoffmann, R.; Woodward, R. B. Conservation of Orbital Symmetry. *Acc. Chem. Res.* **1968**, *1*, 17−22.
(47) Li, Z.; Anderson, S. L. Pyrolysis Chemistry of Cubane and Methylcubane: The Effect of Methyl Substitution on Stability and Product Branching. *J. Phys. Chem. A* **2003**, *107*, 1162−1174.
(48) Leinenweber, K. D.; Tyburczy, J. A.; Sharp, T. G.; Soignard, E.; Diedrich, T.; Petuskey, W. B.; Wang, Y.; Mosenfelder, J. L. Cell Assemblies for Reproducible Multi-Anvil Experiments (the COMPRES Assemblies). *Am. Mineral.* **2012**, *97*, 353−368.
(49) Prescher, C.; Prakapenka, V. B. DIOPTAS: A Program for Reduction of Two-Dimensional X-Ray Diffraction Data and Data Exploration. *High Pressure Res.* **2015**, *35*, 223−230.
(50) Kresse, G.; Furthmüller, J. Efficient Iterative Schemes for Ab Initio Total-Energy Calculations Using a Plane-Wave Basis Set. *Phys. Rev. B: Condens. Matter Mater. Phys.* **1996**, *54*, 11169−11186.
(51) Perdew, J. P.; Burke, K.; Ernzerhof, M. Generalized Gradient Approximation Made Simple. *Phys. Rev. Lett.* **1996**, *77*, 3865−3868.
(52) Perdew, J. P.; Burke, K.; Ernzerhof, M. Generalized Gradient Approximation Made Simple [Phys. Rev. Lett. 77, 3865 (1996)]. *Phys. Rev. Lett.* **1997**, *78*, 1396.
(53) Blöchl, P. E. Projector Augmented-Wave Method. *Phys. Rev. B: Condens. Matter Mater. Phys.* **1994**, *50*, 17953−17979.
(54) Kresse, G.; Joubert, D. From Ultrasoft Pseudopotentials to the Projector Augmented-Wave Method. *Phys. Rev. B: Condens. Matter Mater. Phys.* **1999**, *59*, 1758−1775.
(55) Grimme, S.; Antony, J.; Ehrlich, S.; Krieg, H. A Consistent and Accurate Ab Initio Parametrization of Density Functional Dispersion Correction (DFT-D) for the 94 Elements H-Pu. *J. Chem. Phys.* **2010**, *132*, 154104.
(56) Grimme, S.; Ehrlich, S.; Goerigk, L. Effect of the Damping Function in Dispersion Corrected Density Functional Theory. *J. Comput. Chem.* **2011**, *32*, 1456−1465.
(57) Martoňák, R.; Laio, A.; Parrinello, M. Predicting Crystal Structures: The Parrinello-Rahman Method Revisited. *Phys. Rev. Lett.* **2003**, *90*, 75503.
(58) Yildirim, T.; Gehring, P. M.; Neumann, D. A.; Eaton, P. E.; Emrick, T. Unusual Structure, Phase Transition, and Dynamics of Solid Cubane. *Phys. Rev. Lett.* **1997**, *78*, 4938−4941.
(59) Kaszynski, P.; Friedli, A. C.; Michl, J. Toward a Molecular-Size Tinkertoy Construction Set. Preparation of Terminally Functionalized [n]Staffanes from [1.1.1]Propellane. *J. Am. Chem. Soc.* **1992**, *114*, 601−620.
(60) Boultif, A.; Louër, D. Powder Pattern Indexing with the Dichotomy Method. *J. Appl. Crystallogr.* **2004**, *37*, 724−731.
(61) Wilhelm, C.; Boyd, S. A.; Chawda, S.; Fowler, F. W.; Goroff, N. S.; Halada, G. P.; Grey, C. P.; Lauher, J. W.; Luo, L.; Martin, C. D.; Parise, J. B.; Tarabrella, C.; Webb, J. A. Pressure-Induced Polymerization of Diiodobutadiyne in Assembled Cocrystals. *J. Am. Chem. Soc.* **2008**, *130*, 4415−4420.
(62) Fleischer, E. B. X-Ray Structure Determination of Cubane. *J. Am. Chem. Soc.* **1964**, *86*, 3889−3890.
(63) Walters, J. K.; Newport, R. J.; Howells, W. S.; Bushnell-Wye, G. Neutron and X-Ray Diffraction Studies of a-C:N:H. *J. Phys.: Condens. Matter* **1996**, *8*, 4739−4750.
(64) Anikeenko, A. V.; Kim, A. V.; Medvedev, N. N. Molecular Dynamics Simulation of the Structure of C6 Alkanes. *J. Struct. Chem.* **2010**, *51*, 1090−1096.
(65) Falkowska, M.; Bowron, D. T.; Manyar, H. G.; Hardacre, C.; Youngs, T. G. A. Neutron Scattering of Aromatic and Aliphatic Liquids. *ChemPhysChem* **2016**, *17*, 2043−2055.
(66) Juhl, S. J.; Wang, T.; Vermilyea, B.; Li, X.; Crespi, V. H.; Badding, J. V.; Alem, N. Local Structure and Bonding of Carbon Nanothreads Probed by High-Resolution Transmission Electron Microscopy. *J. Am. Chem. Soc.* **2019**, *141*, 6937−6945.
(67) Huang, H.; Ward, M. D.; Juhl, S. J.; Biswas, A.; Alem, N.; Badding, J. V.; Strobel, T. A. Low-Dose Transmission Electron Microscopy of Highly-Oriented Polyacetylene. *Microsc. Microanal.* **2018**, *24*, 2030−2031.
(68) Kuei, B.; Aplan, M. P.; Litofsky, J. H.; Gomez, E. D. New Opportunities in Transmission Electron Microscopy of Polymers. *Mater. Sci. Eng., R* **2020**, *139*, 100516.
(69) Seyring, M.; Simon, A.; Voigt, I.; Ritter, U.; Rettenmayr, M. Quantitative Crystallographic Analysis of Individual Carbon Nanofibers Using High Resolution Transmission Electron Microscopy and Electron Diffraction. *Carbon* **2017**, *116*, 347−355.
(70) Kuei, B.; Gomez, E. D. Elucidating Mechanisms for Electron Beam Damage in Conjugated Polymers. *Microsc. Microanal.* **2018**, *24*, 1988−1989.
(71) Chien, J. C. W.; Karasz, F. E.; Shimamura, K. Crystal Structure of Pristine and Iodine-Doped Cis-Polyacetylene. *Macromolecules* **1982**, *15*, 1012−1017.
(72) Juhl, S.; Li, X.; Badding, J.; Alem, N. Low Dose Characterization of Diamondoid Carbon Nanothreads by Transmission Electron Microscopy. *Microsc. Microanal.* **2017**, *23*, 1846−1847.
(73) Orth, V. H.; Fischer, E. W. Änderungen Der Gitterstruktur Hochpolymerer Einkristalle Durch Bestrahlung Im Elektronenmikroskop. *Makromol. Chem.* **1965**, *88*, 188−214.
(74) Mikkelsen, K. V.; Ratner, M. A. Electron Tunneling in Solid-State Electron-Transfer Reactions. *Chem. Rev.* **1987**, *87*, 113−153.
(75) Diederich, F.; Kivala, M. All-Carbon Scaffolds by Rational Design. *Adv. Mater.* **2010**, *22*, 803−812.
(76) Sun, J.; Dong, X.; Wang, Y.; Li, K.; Zheng, H.; Wang, L.; Cody, G. D.; Tulk, C. A.; Molaison, J. J.; Lin, X.; Meng, Y.; Jin, C.; Mao, H.-K. Pressure-Induced Polymerization of Acetylene: Structure-Directed Stereoselectivity and a Possible Route to Graphane. *Angew. Chem.* **2017**, *129*, 6653−6657.
(77) Wen, X.-D.; Hand, L.; Labet, V.; Yang, T.; Hoffmann, R.; Ashcroft, N. W.; Oganov, A. R.; Lyakhov, A. O. Graphane Sheets and

https://dx.doi.org/10.1021/jacs.9b12352
J. Am. Chem. Soc. 2020, 142, 17944−17955

Crystals under Pressure. *Proc. Natl. Acad. Sci. U. S. A.* **2011**, *108*, 6833−6837.
(78) Lian, C.-S.; Wang, X.-Q.; Wang, J.-T. Hydrogenated K4 Carbon: A New Stable Cubic Gauche Structure of Carbon Hydride. *J. Chem. Phys.* **2013**, *138*, 024702.
(79) He, C.; Sun, L. Z.; Zhang, C. X.; Zhong, J. Low Energy Three-Dimensional Hydrocarbon Crystal from Cold Compression of Benzene. *J. Phys.: Condens. Matter* **2013**, *25*, 205403.
(80) Lian, C.-S.; Li, H.-D.; Wang, J.-T. Crystalline Structures of Polymeric Hydrocarbon with 3,4-Fold Helical Chains. *Sci. Rep.* **2015**, *5*, 7723.
(81) Brazhkin, V. V; Nikolaev, N. A.; Shulga, Y. M.; Lebed, Y. B.; Kondrin, M. V. The Structure and Synthesis of Organic Crystalline Polymers: Hints from Ab Initio Computation. *CrystEngComm* **2018**, *20*, 4003−4011.
(82) Thess, A.; Lee, R.; Nikolaev, P.; Dai, H.; Petit, P.; Robert, J.; Xu, C.; Lee, Y. H.; Kim, S. G.; Rinzler, A. G.; Colbert, D. T.; Scuseria, G. E.; Tomanek, D.; Fischer, J. E.; Smalley, R. E. Crystalline Ropes of Metallic Carbon Nanotubes. *Science* **1996**, *273*, 483−487.
(83) Petkov, V.; Zavalij, P. Y.; Lutta, S.; Whittingham, M. S.; Parvanov, V.; Shastri, S. Structure beyond Bragg: Study of V2O5 Nanotubes. *Phys. Rev. B: Condens. Matter Mater. Phys.* **2004**, *69*, 085410.
(84) Prill, D.; Juhas, P.; Billinge, S. J. L.; Schmidt, M. U. Towards Solution and Refinement of Organic Crystal Structures by Fitting to the Atomic Pair Distribution Function. *Acta Crystallogr., Sect. A: Found. Adv.* **2016**, *72*, 62−72.
(85) Ciabini, L.; Santoro, M.; Gorelli, F. A.; Bini, R.; Schettino, V.; Raugei, S. Triggering Dynamics of the High-Pressure Benzene Amorphization. *Nat. Mater.* **2007**, *6*, 39−43.
(86) Zhu, L.; Cohen, R. E.; Strobel, T. A. Phase Transition Pathway Sampling via Swarm Intelligence and Graph Theory. *J. Phys. Chem. Lett.* **2019**, *10*, 5019−5026.
(87) Xu, E.; Lammert, P. E.; Crespi, V. H. Systematic Enumeration of sp3 Nanothreads. *Nano Lett.* **2015**, *15*, 5124−5130.
(88) Liu, M.; Artyukhov, V. I.; Lee, H.; Xu, F.; Yakobson, B. I. Carbyne from First Principles: Chain of C Atoms, a Nanorod or a Nanorope. *ACS Nano* **2013**, *7*, 10075−10082.
(89) Lu, J. P. Elastic Properties of Carbon Nanotubes and Nanoropes. *Phys. Rev. Lett.* **1997**, *79*, 1297−1300.
(90) Segall, D. E.; Ismail-Beigi, S.; Arias, T. A. Elasticity of Nanometer-Sized Objects. *Phys. Rev. B: Condens. Matter Mater. Phys.* **2002**, *65*, 214109.
(91) Demingos, P. G.; Muniz, A. R. Electronic and Mechanical Properties of Partially Saturated Carbon and Carbon Nitride Nanothreads. *J. Phys. Chem. C* **2019**, *123*, 3886−3891.

https://dx.doi.org/10.1021/jacs.9b12352
J. Am. Chem. Soc. 2020, 142, 17944−17955